Applied Physics A (2023) 129:728
https://doi.org/10.1007/s00339-023-07005-1

Applied Physics A
Materials Science & Processing

Ion-gated tungsten oxide based electrochemical transistors with subthreshold slopes approaching the thermodynamic limit

Kaiyuan Zhang[1] · Wenxin Zhao[1] · Xing Sheng[1]

Received: 19 June 2023 / Accepted: 13 September 2023

Abstract
Electrochemical transistors (ECTs) are switches that are controlled by ionic gating, and find emerging applications in electronic devices and chemical sensors. In this paper, we fabricate microscale tungsten oxide (WO_x) ECTs and study their subthreshold characteristics. We optimize the film deposition process to produce WO_x films with various oxygen concentrations, and investigate their physical and chemical properties. We employ transparent amorphous WO_3 films as the channel material for ECTs, and experimentally investigate their subthreshold behaviors by injecting different metal ions in electrolytes. In addition, we explore the dynamic response of the WO_3 ECT. Gated by cation intercalation, we find that these WO_3 ECTs can obtain a subthreshold slope as low as 60 mV/dec at room temperature, approaching the same thermodynamic limit as field-effect transistors. The material and device strategies provide a route to realizing future computing and sensing devices.

Keywords Electrochemical transistor · Subthreshold slope · Tungsten oxide · Ion intercalation

1 Introduction

Since their invention, silicon-based complementary metal–oxide–semiconductor (CMOS) transistors, or metal–oxide–semiconductor field-effect transistors (MOSFETs), have been serving as the cornerstone of modern integrated circuits. In the past few decades, the integrated circuit industry began to take the highway of production and application from scientific research. The evolution of MOSFETs has been following the Moore's law [1], which predicts that the transistors continue to be smaller, faster, and more energy efficient, providing computing systems with higher capacity and efficacy [2–4]. To further scale down the transistors and improve the circuit performance, new device architectures have been continuously developed. Representative examples include fin field-effect transistors (FinFETs) [5, 6] and gate-all-around field-effect transistors (GAAFETs) [7, 8]. Nowadays, state-of-the-art CMOS transistors have geometries scaled down to the nanometer scale and approaching the physical limit [9], and device concepts based on novel channel semiconductors like 2D materials have been proposed to further reduce the device footprint [10].

On the other hand, electrochemical transistors (ECTs) have semiconductor channels whose conductivity is modulated by ions rather than electrons. In these ECTs, external electrical fields are applied in an electrolyte, inject mobile metallic cations into the channels, dope the channel material and alter its conductance [11, 12]. The channel components comprise organic compounds like poly(3,4-ethylenedioxythiophene) polystyrene sulfonate (PEDOT:PSS) [13] or inorganic materials including tungsten oxide (WO_x) and molybdenum oxide [14]. Their intercalation based operation mechanism is fundamentally different from that of conventional field-effect transistors (FETs), and has drawn considerable attention in areas like neuromorphic computing, chemical and biological sensing [15–20]. Similar to traditional FETs, the subthreshold slope (*SS*) of ECTs should be above $kT \cdot \ln 10/q \approx 60$ mV/dec at room temperature ($T = 300$ K), dictated by the Boltzmann limit [21]. However, few works have investigates the subthreshold behaviors of these ECT devices, and most works merely focus on the linear and saturation regions of ECTs, with lithium (Li^+) as the injected cation [22–25]. A recent study reports a

✉ Xing Sheng
xingsheng@tsinghua.edu.cn

[1] Department of Electronic Engineering, Beijing National Research Center for Information Science and Technology, Institute for Precision Medicine, Center for Flexible Electronics Technology, IDG/McGovern Institute for Brain Research, Tsinghua University, Beijing 100084, China

Published online: 25 September 2023

well-designed organic ECT based on a special organic channel can have an *SS* approaching 60 mV/dec [26]. Nevertheless, subthreshold characteristics of inorganic based ECTs have not yet been systematically investigated. In addition, most reported intercalation processes in inorganic ECTs are based on Li^+ cation, but subthreshold behaviors of these devices injected with different ions remain unexplored, either. We envision that studying the subthreshold properties of inorganic ECTs would create vast opportunities in the development of novel sensing and computing devices.

In this work, we exploit the subthreshold behaviors of a WO_x based ECT, under the injection of different metallic cations. We lithographically define microscale WO_x ECTs, and experimentally investigate their physical and chemical characteristics. In particular, we systematically measure the subthreshold properties of the WO_x ECT intercalated with various ions, and find that the designed device has an *SS* approaching 60 mV/dec at room temperature. Finally, we examine the temporal response of the device.

2 Materials and methods

Figure 1a illustrates the structure and fabrication process to produce the WO_x-based ECT devices. First, glass substrates are immersed in a mixture of ammonia and hydrogen peroxide in deionized (DI) water (1:1:5) solution at 70 °C for cleaning for 10 min, and then washed with acetone, isopropyl alcohol and DI water, respectively. Subsequently, a photoresist layer (AZ nLof 2070, Microchemicals) is spin-coated on the cleaned glass substrate. After baking the solvent, ultraviolet light (365 nm i-Line) exposes the photoresist through a chrome photomask, and the electrode pattern of the device is obtained by immersing the sample in the alkaline developer (MIF-300). Under the condition of argon (Ar) (power 32 W, pressure 0.25 Pa, Ar flow 40 sccm, deposition rate 10 nm/min), chrome/gold (Cr/Au) films with thicknesses of about 10 nm/100 nm are deposited by DC magnetron sputtering. After lifting off the photoresist in acetone, patterned Cr/Au films are obtained as the source and drain electrodes. A similar process is applied to fabricate patterned WO_x films on top of Cr/Au electrodes. Specifically, a WO_x film (thickness ~ 100 nm) is grown by DC magnetron sputtering with a pure tungsten (W) target in a mixture of argon (Ar) and oxygen (O_2) gases (power 60 W, pressure 2.5 Pa, Ar flow

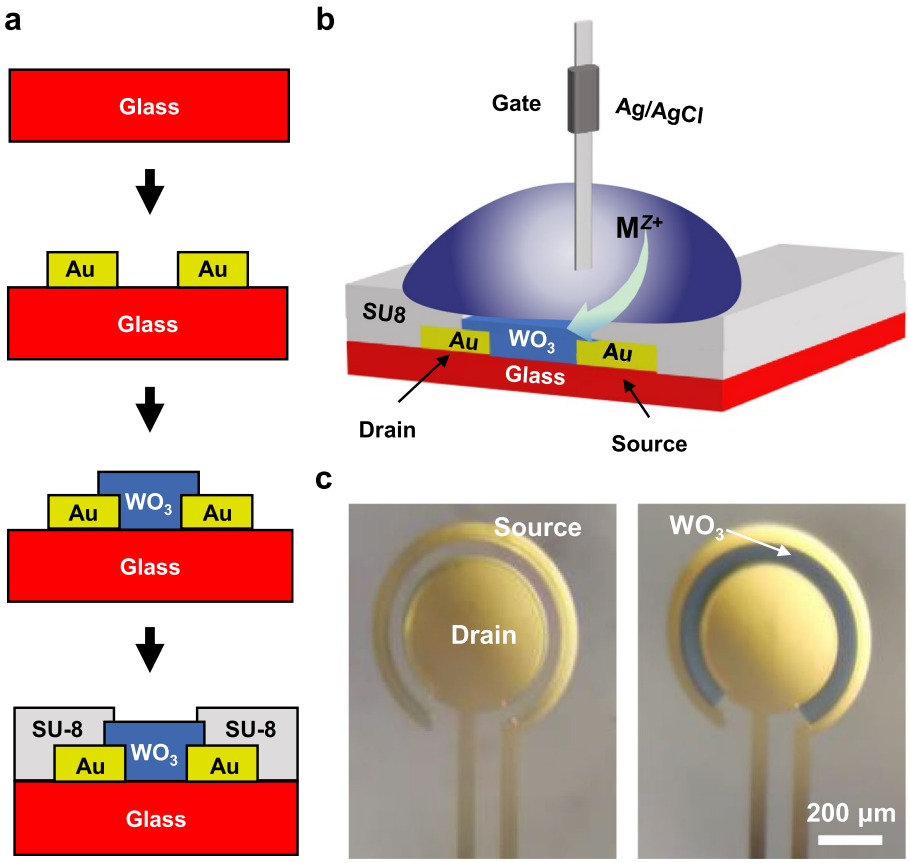

Fig. 1 **a** Schematic illustration of the process flow to fabricate the WO_x based electrochemical transistor (ECT) devices. **b** 3D cartoon illustration of the intercalation process for the ECT in an aqueous solution containing cations (M^{Z+}), with a Ag/AgCl wire as the gate electrode. **c** Microscopic photos showing an ECT before (top) and after (bottom) cation intercalation

40 sccm, O_2 flow varying from 0 to 40 sccm, deposition rate ~ 10 nm/min). Finally, an epoxy layer (thickness ~ 5 µm, SU-8 3005, Microchemicals) is lithographically patterned and protects the Cr/Au electrode film against the electrolyte.

Shown in Fig. 1b, the WO_x ECT is operated when immersed into a liquid electrolyte made of a propylene carbonate (PC) solution containing different metal cations (M^{Z+}). A silver/silver chloride (Ag/AgCl) wire inserts into the electrolyte as the gate electrode. Under an applied bias voltage (V_g), metal ions are intercalated into or extracted from the WO_x channel and alter the channel conductance, via the redox reaction [27, 28]:

$$WO_x + M^{Z+} + Ze^- \underset{\text{extraction}}{\overset{\text{intercalation}}{\rightleftharpoons}} MWO_x.$$

Following the reaction, the valence state of W varies between the high level W^{6+} and the low level W^{5+}, resulting in the WO_x channel's color change between the transparent state and the blue state, as shown in captured photos (Fig. 1c). Shown in Fig. 1c, the WO_x ECT has a channel length of about 50 µm, and a circular shaped WO_x channel layer is designed to increase the channel width to more than 1 mm, thereby increase the channel conductance.

3 Results

We further characterize physical and chemical properties of the as-deposited WO_x film under different conditions. Different WO_x films are formed by sputtering a pure W target in different gas environments. During the sputtering process, the flow of Ar gas is fixed at 40 sccm, while the flow of O_2 gas is adjusted from 0 to 40 sccm to vary the valence state of W. Figure 2a shows WO_x films deposited on glass under different Ar:O_2 ratios (40:0, 40:10, 40:20 and 40:40, in the unit of sccm). Sputtering with pure Ar gas (Ar:O_2 = 40:0) produces a pure and opaque metallic W film. The addition of O_2 gas causes the oxidation of W (forms WO_x) and enhances the film transparency in the visible range (Fig. 2b). The optical transmittance spectra for these different W and WO_x films are characterized from 300 to 800 nm at normal incidence, by using a ultraviolet–visible-infrared spectrometer (CARY 5000, Agilent). The band gap energy of these WO_x films is determined by the Tauc-plot method and around 3.58 eV, consistent with reported data [29]. X-ray diffraction (XRD) patterns in Fig. 2c reveal β-phase W (for Ar:O_2 = 40:0) and amorphous states of WO_x films (for Ar:O_2 = 40:10, 40:20 and 40:40). The measured sheet resistances for these four samples in Fig. 2a are 27×10^{-9}, 1.8, 12 and 13 MΩ/sq, respectively (Fig. 2d). As demonstrated in the subsequent section, the gas flow of Ar:O_2 = 40:40 creates the WO_x film with the highest valence state (approaching 6+) for W, which has the highest transparency in the visible spectral range, as well as the lowest electrical conductivity. As shown in Fig. 1c, through the intercalation process by applying a forward bias through the electrolyte, metallic cations like Li^+ can be injected into the WO_x film, reducing its transparency and increasing its electrical conductivity, both due to the generation of extra free carriers in the intercalated WO_x film.

X-ray photoelectron spectroscopic (XPS) measurements further reveal the chemical state of WO_x films (Fig. 3). Figure 3a plots the W 4f core-level XPS results for four different samples. The measured spectra (red curves) are fitted using four different colored curves, of which blue, green, cyan and purple ones represent elementary W, W^{4+}, W^{5+} and W^{6+} ionic states, respectively [30]. Associated binding energy peaks are 31.6 eV and 33.8 eV for W, 33.1 eV and 35.3 eV for W^{4+}, 36.1 eV and 38.3 eV for W^{5+}, 35.4 eV and 37.6 eV for W^{6+}. Black curves present the overall fitting results that match the experimental data (red curves).

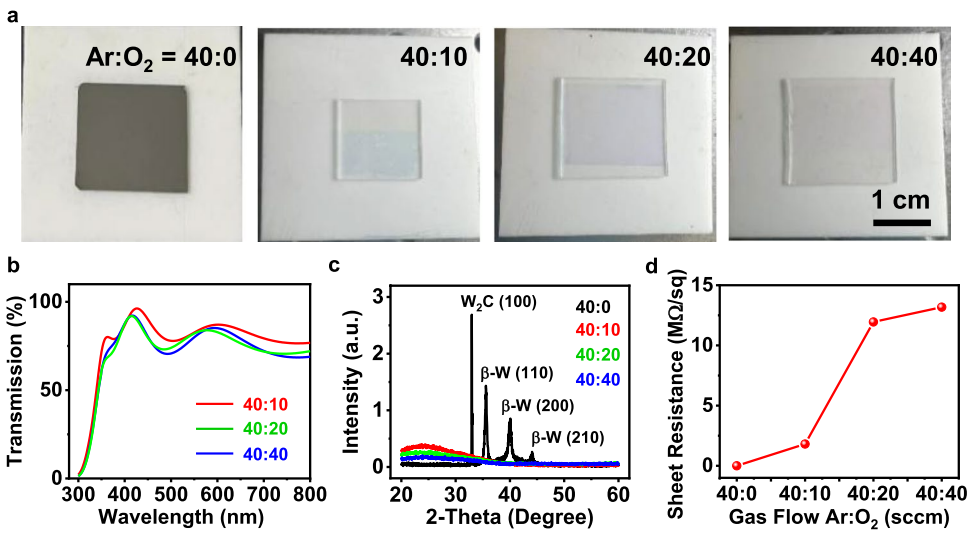

Fig. 2 **a** Photographs showing sputtered WO_x films with different gas flows. From left to right, flow of Ar:O_2 = 40:0, 40:10, 40:20, 40:40 (unit: sccm). **b** Optical transmission spectra of WO_x deposited with different O ratio. Ar:O_2 = 40:10 (red), 40:20 (green), 40:40 (blue). **c** XRD spectra for WO_x deposited with different O ratio. Ar:O_2 = 40:0 (black), 40:10 (red), 40:20 (green), 40:40 (blue). The W_2C (100) peak is probably originated from the carbon contamination in the W film [31]. **d** Measured sheet resistance for WO_x deposited with different O ratio

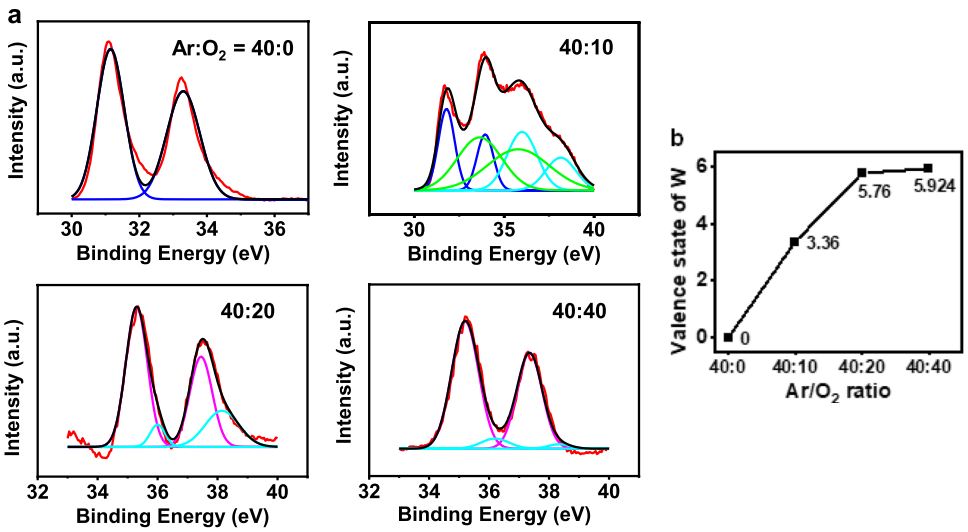

Fig. 3 **a** XPS W_{4f} wide angle spectra of WO_x deposited with different O_2 ratio. Ar:O_2 = 40:0, 40:10, 40:20, 40:40. Red and black curves are for the original data and fitting results, respectively. Blue, green, cyan and purple curves correspond to W, W^{4+}, W^{5+} and W^{6+}, respectively. **b** Valence state of W at different sputtering conditions

Based on the fitting data, corresponding valence states of W for different films are calculated by weighting the integral of different peaks, and plotted in Fig. 3b. First, the film deposited without O_2 gas only contains peaks for elementary W. The W valence state increases associated with the additional O_2 gas during sputtering. The WO_x film deposited at Ar:O_2 = 40:10 contains W, W^{4+} and W^{5+}, with a W valence state of 3.36. At Ar:O_2 = 40:20, metallic W and W^{4+} disappear, and only W^{5+} and W^{6+} remain in the film (valence state = 5.76). At Ar:O_2 = 40:40, almost all the W atoms are completely oxidized and become W^{6+} (valence state = 5.924), resulting a tungsten trioxide (WO_3) film with the highest transparency and the lowest electrical conductance among all the samples.

The fully oxidized WO_3 film, which exhibit the highest visible transparency and electrical resistivity, is utilized to form the channel of the ECT device shown in Fig. 1. In Fig. 4a, b, we study its subthreshold behaviors during intercalation. While similar WO_3 or other metal oxides based ECT devices have been reported previously, their SS parameters have not been analyzed. Here, different metallic cations (Li^+, K^+, Mg^{2+}, Zn^{2+}, Ba^{2+}, or Al^{3+}) are mixed into the PC electrolyte with the same concentration of 1 mol/L. A droplet of electrolyte is placed on the ECT, and

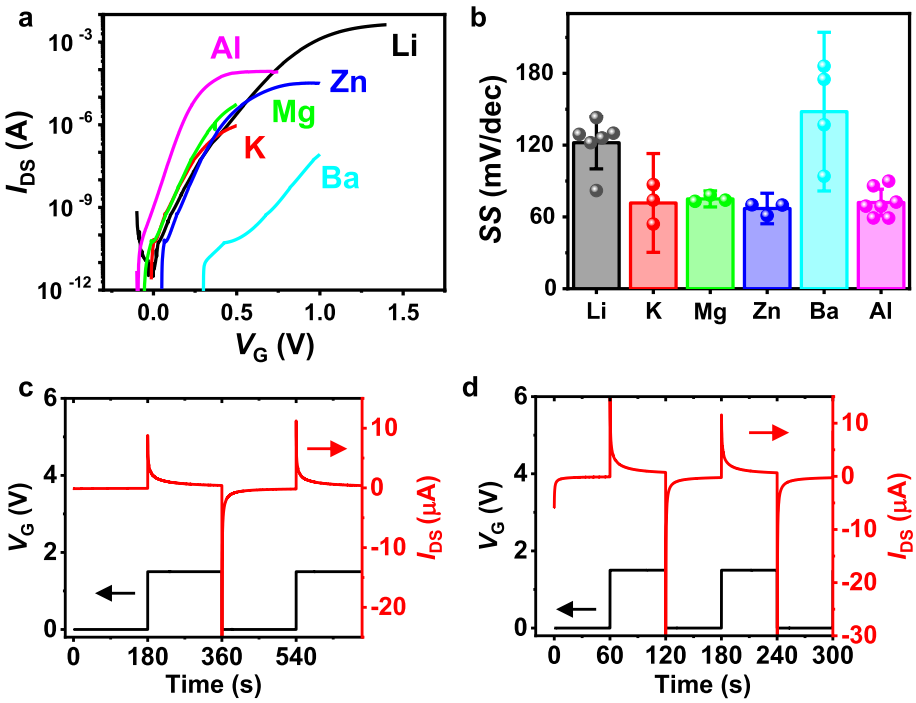

Fig. 4 **a** Transfer characteristics of a typical WO_3 ECT with the intercalation of different cations: Li^+ (black), K^+ (red), Mg^{2+} (green), Zn^{2+} (blue), Ba^{2+} (cyan) and Al^{3+} (purple). **b** Measured subthreshold slopes (SS) for the WO_x ECT with the intercalation with different metal ions. Sample numbers are n = 6, 3, 3, 3, 4 and 7 for Li, K, Mg, Zn, Ba and Al, respectively. **c**, **d** Dynamic response of drain–source current (I_{DS}) for the WO_x ECT under a cyclic gate voltage (V_G = 0 or 1.5 V) with a period of **c** 180 s and **d** 60 s. Here the drain–source voltage (V_{DS}) is kept at 0.5 V

the gate voltage (V_G) is supplied with a Ag/AgCl electrode. Via a semiconductor parameter analyzer (Keithley 4200A-SCS, Tektronix), V_G is scanned from − 0.5 to + 1.5 V at a sweeping rate of 1 mV/s, and the supplied voltage between the drain and source electrodes (V_{DS}) is set to 0.5 V. Figure 4a plots transfer characteristics of the WO_3 ECT when injected by different metal ions at room temperature. Around $V_G = 0$ V, the measured drain–source current (I_{DS}) follows a classical logarithmic function of V_G. The *SS* results of the ECT are calculated based on I_{DS} in the range between 10^{-9} and 10^{-3} A. In Fig. 4b, statistical analyses based on multiple repetitive measurements show that obtained SS are 122 ± 20, 72 ± 20, 75 ± 3, 67 ± 6, 148 ± 50, and 72 ± 18 mV/dec, for the intercalation of Li^+, K^+, Mg^{2+}, Zn^{2+}, Ba^{2+} and Al^{3+}, respectively. We can clearly see that the SS of microscale WO_3 ECT can approach the thermodynamic limit (kT•ln10/q ≈ 60 mV/dec) when intercalated with cations like K^+, Mg^{2+}, Zn^{2+} or Al^{3+}. Conventionally, Li^+ is commonly used for intercalation in ECTs, because of its small atomic size and fast dynamics in ionic solids. However, here we find that the SS of microscale WO_3 ECT is relatively large (122 ± 20 mV/dec) when intercalated with Li^+, which is likely due to the fact that Li^+ can lead to a large leakage current by ion insertion [32]. Additionally, devices injected with Ba^{2+} also possess a relatively high SS (148 ± 50 mV/dec) and a large variance, and this is because that compared to other ions, the large size of Ba^{2+} makes it difficult to be inserted into the WO_3 [33]. Furthermore, the large size of Ba^{2+} also causes a positive offset (around + 0.3 V) of the turn-on voltage compared to other ions.

We further explore the dynamic response of the WO_3 ECT under cyclic Li^+ intercalation and extraction. At $V_{DS} = 0.5$ V, I_{DS} is measured by applying a square-wave V_G signal voltage of 0 V and 1.5 V at the minimum and the maximum. Figures 4c, d plot recorded temporal I_{DS} signals with wave periods of 360 s and 120 s, respectively. When V_G is switched from 0 to 1.5 V or vice versa, the device experience a prompt I_{DS} increase or decrease, which is probably associated with the capacitive charge or discharge within the electrolyte. Due to the poor conductivity of the solvent PC, the operating current was reversed when the VG was suddenly switched to a high voltage. After nearly 1 min of stability, I_{DS} gradually falls back to the stable state, and the current at this time is larger than that in the low-voltage region. I_{DS} stabilizes after charging for about 1 min, when the Li^+ intercalation reaches a saturation state. The temporal response of the WO_3 ECT is much slower than that of PEDOT:PSS organic ECT operated in an aqueous solution [34], due to the slow diffusion of cations in the PC electrolyte and WO_3. Its dynamic performance can be further improved by introducing electrolytes with higher cation diffusivities or optimizing the structure of the WO_3 channel.

4 Conclusion

In this work, we design and fabricate microscale WO_3 ECT devices and characterize their subthreshold performance. The physical and chemical properties of WO_x films are analyzed and optimized under different deposition conditions. Their behaviors under injection with different cations are systematically exploited. We demonstrate that these devices can approach SS of 60 mV/dec when intercalated with certain cations (for example, K^+, Mg^{2+}, Zn^{2+} and Al^{3+}). While Li^+ is the most commonly used cation for intercalation in WO_x because of its better reversibility and switching speed, its SS is not optimal due to the large leakage. Therefore, one must consider the trade-offs between the SS and other operational device characteristics. The current device has limited dynamic response (timescale of a few seconds), which is inferior to that of the organic (for example, PEDOT:PSS) based ECT (with a response time of micro- to milli-seconds). The device dynamic response can be further improved by optimizing the device geometry and structure, for example, by the design of nanostructured channel layer. In addition, solid-based electrolyte can be implemented to realize fully integrated solid-state ECT devices. Although there are still challenges associated with the device application, including its switching speed, reversibility and stability, our results show that these ion gated devices are constrained by the same thermodynamic limit as classical transistors, and implicate potentials in the future logic and sensing devices.

Author contributions Conceptualization, KZ and XS; methodology, KZ, WZ and XS; writing—original draft preparation, KZ; writing—review and editing, XS; supervision, XS; project administration, XS; funding acquisition, XS. All authors have read and agreed to the published version of the manuscript.

Funding This work is supported by Tsinghua University Initiative Scientific Research Program (20211080065), Beijing Municipal Natural Science Foundation (Z220015) and National Natural Science Foundation of China (NSFC) (52272277).

Data availability The data that support the findings of this study are available from the corresponding author (Xing Sheng) upon reasonable request.

Declarations

Conflict of interest The authors declare no conflict of interest. The funders had no role in the design of the study; in the collection, analyses, or interpretation of data; in the writing of the manuscript; or in the decision to publish the results.

References

1. G.E. Moore, Cramming more components onto integrated circuits (reprinted from Electronics, pp. 114–117, April 19, 1965) [J]. Proc. IEEE **86**(1), 82–85 (1998)

2. R.H. Dennard, F.H. Gaensslen, H.N. Yu et al., Design of ion-implanted Mosfet's with very small physical dimensions (reprinted from IEEE Journal of Solid-State Circuits, Vol 9, pp. 256–268, 1974) [J]. Proc. IEEE **87**(4), 668–678 (1999)
3. R. Feynman, *There's Plenty of Room at the Bottom [M]* (CRC Press, Boca Raton, 2018)
4. J.-A. Carballo, W.-T.J. Chan, P.A. Gargini, et al., Itrs 2.0: toward a re-framing of the semiconductor technology roadmap, in *Proceedings of the 32nd IEEE International Conference on Computer Design (ICCD), Seoul, SOUTH KOREA, F 2014 Oct 19–22, 2014 [C]* (2014)
5. D. Hisamoto, W.C. Lee, J. Kedzierski et al., FinFET—a self-aligned double-gate MOSFET scalable to 20 Nm [J]. IEEE Trans. Electron Devices **47**(12), 2320–2325 (2000)
6. B. Yu, L.L. Chang, S. Ahmed, et al., FinFET scaling to 10 nm gate length, in *Proceedings of the IEEE International Electron Devices Meeting, San Francisco, Ca, F 2002 Dec 08–11, 2002 [C]* (2002)
7. Y.C. Huang, M.H. Chiang, S.J. Wang et al., GAAFET versus pragmatic FinFET at the 5 nm Si-based CMOS technology node [J]. IEEE J. Electron Devices Soc. **5**(3), 164–169 (2017)
8. D. Yakimets, G. Eneman, P. Schuddinck et al., Vertical GAAFETS for theu CMOS scaling [J]. IEEE Trans. Electron Devices **62**(5), 1433–1439 (2015)
9. I. Ferain, C.A. Colinge, J.P. Colinge, Multigate transistors as the future of classical metal-oxide-semiconductor field-effect transistors [J]. Nature **479**(7373), 310–316 (2011)
10. M. Chhowalla, D. Jena, H. Zhang, Two-dimensional semiconductors for transistors [J]. Nat. Rev. Mater. **1**(11), 1–15 (2016)
11. R. Baughman, L. Shacklette, R. Elsenbaumer, E. Plichta, C. Becht, Conducting polymer electromechanical actuators, in *Conjugated Polymeric Materials: Opportunities in Electronics, Optoelectronics, and Molecular Electronics* (1990), pp. 559–582. https://doi.org/10.1007/978-94-009-2041-5
12. D.A. Bernards, G.G. Malliaras, Steady-state and transient behavior of organic electrochemical transistors. Adv. Funct. Mater.Funct. Mater. **17**(17), 3538–3544 (2007). https://doi.org/10.1002/adfm.200601239
13. J. Rivnay, S. Inal, A. Salleo, R.M. Owens, M. Berggren, G.G. Malliaras, Organic electrochemical transistors. Nat. Rev. Mater. **3**(2), 17086 (2018). https://doi.org/10.1038/natrevmats.2017.86
14. S. Balendhran et al., Field effect biosensing platform based on 2D α-MoO3. ACS Nano **7**(11), 9753–9760 (2013). https://doi.org/10.1021/nn403241f
15. M. Kaisti, Detection principles of biological and chemical FET sensors. Biosens. Bioelectron. **98**, 437–448 (2017). https://doi.org/10.1016/j.bios.2017.07.010
16. S. Hong et al., FET-type gas sensors: a review. Sens. Actuators B Chem. **330**, 129240 (2021). https://doi.org/10.1016/j.snb.2020.129240
17. J. Zhang, L. Liu, Y. Yang, Q. Huang, D. Li, D. Zeng, A review on two-dimensional materials for chemiresistive-and FET-type gas sensors. Phys. Chem. Chem. Phys. **23**(29), 15420–15439 (2021). https://doi.org/10.1039/D1CP01890F
18. L. Torsi, M. Magliulo, K. Manoli, G. Palazzo, Organic field-effect transistor sensors: a tutorial review. Chem. Soc. Rev. **42**(22), 8612–8628 (2013). https://doi.org/10.1039/C3CS60127G
19. C. Dai, Y. Liu, D. Wei, Two-dimensional field-effect transistor sensors: the road toward commercialization. Chem. Rev. **122**(11), 10319–10392 (2022). https://doi.org/10.1021/acs.chemrev.1c00924
20. C.-S. Lee, S.K. Kim, M. Kim, Ion-sensitive field-effect transistor for biological sensing. Sensors **9**(9), 7111–7131 (2009). https://doi.org/10.3390/s90907111
21. J.-P. Colinge, Subthreshold slope of thin-film SOI MOSFET's. IEEE Electron Device Lett. **7**(4), 244–246 (1986). https://doi.org/10.1109/EDL.1986.26359
22. K. Gopalakrishnan, P.B. Griffin, J.D. Plummer, I-MOS: a novel semiconductor device with a subthreshold slope lower than kT/q, in *Digest. International Electron Devices Meeting* (IEEE, 2002), pp. 289–292. https://doi.org/10.1109/IEDM.2002.1175835
23. W.Y. Choi, B.-G. Park, J.D. Lee, T.-J.K. Liu, Tunneling field-effect transistors (TFETs) with subthreshold swing (SS) less than 60 mV/dec. IEEE Electron Device Lett. **28**(8), 743–745 (2007). https://doi.org/10.1109/LED.2007.901273
24. G.A. Salvatore, L. Lattanzio, D. Bouvet, I. Stolichnov, N. Setter, A.M. Ionescu, Ferroelectric transistors with improved characteristics at high temperature. Appl. Phys. Lett. **97**(5), 053503 (2010). https://doi.org/10.1063/1.3467471
25. Q. Huang, R. Huang, Y. Pan, S. Tan, Y. Wang, Resistive-gate field-effect transistor: a novel steep-slope device based on a metal—insulator—metal—oxide gate stack. IEEE Electron Device Lett. **35**(8), 877–879 (2014). https://doi.org/10.1109/LED.2014.2327219
26. V. Venkatraman et al., Subthreshold operation of organic electrochemical transistors for biosignal amplification. Adv. Sci. **5**(8), 1800453 (2018). https://doi.org/10.1002/advs.201800453
27. J.T. Yang et al., Artificial synapses emulated by an electrolyte-gated tungsten-oxide transistor. Adv. Mater. **30**(34), 1801548 (2018). https://doi.org/10.1002/adma.201801548
28. M.S. Barbosa, N. Balke, W.-Y. Tsai, C. Santato, M.O. Orlandi, Structure of the electrical double layer at the interface between an ionic liquid and tungsten oxide in ion-gated transistors. J. Phys. Chem. Lett. **11**(9), 3257–3262 (2020). https://doi.org/10.1021/acs.jpclett.0c00651
29. K. Patel, C. Panchal, V. Kheraj, M. Desai, Growth, structural, electrical and optical properties of the thermally evaporated tungsten trioxide (WO_3) thin films. Mater. Chem. Phys. **114**(1), 475–478 (2009). https://doi.org/10.1016/j.matchemphys.2008.09.071
30. O.Y. Khyzhun, XPS, XES and XAS studies of the electronic structure of tungsten oxides. J. Alloys Compd. **305**(1–2), 1–6 (2000). https://doi.org/10.1016/S0925-8388(00)00697-6
31. A.V. Pervikov, M. Krinitcyn, E.A. Glazkova, N.G. Rodkevich, M.I. Lerner, Synthesis of tungsten carbide from bimodal tungsten powder produced by electrical explosion of wire. Int. J. Refract Metal Hard Mater. **103**, 105733 (2022). https://doi.org/10.1016/j.ijrmhm.2021.105733
32. D. Pasquier, I. Plitz, S. Menocal, G. Amatucci, A comparative study of Li-ion battery, supercapacitor and nonaqueous asymmetric hybrid devices for automotive applications. J. Power. Sources **115**(1), 171–178 (2003). https://doi.org/10.1016/S0378-7753(02)00718-8
33. M. Anderson, S.K. Hurst, Platinum stacking interactions in homoleptic platinum polymers. Eur. J. Inorg. Chem. **2009**(21), 3041–3054 (2009). https://doi.org/10.1002/ejic.200900225
34. M.H. Park, J.H. Li, A. Kumar, G. Li, Y. Yang, Doping of the metal oxide nanostructure and its influence in organic electronics. Adv. Funct. Mater.Funct. Mater. **19**(8), 1241–1246 (2009). https://doi.org/10.1002/adfm.200801639